

Electrochemical Modeling of the Current-Voltage Characteristics of an SOFC in Fuel Cell and Electrolyzer Operation Modes

To cite this article: J.-C. Njodzefon *et al* 2013 *J. Electrochem. Soc.* **160** F313

View the [article online](#) for updates and enhancements.

You may also like

- [Experimental Results of a 10/40 kW-Class Reversible Solid Oxide Cell Demonstration System at Forschungszentrum Jülich](#)
Ro. Peters, W. Tiedemann, I. Hoven et al.
- [Design and partial-load operation of a reversible Solid Oxide Cell system with molten salts thermal storage](#)
Marco Ficili, Paolo Colbertaldo, Giulio Guandalini et al.
- [Defect Chemistry and Transport within Dense \$\text{BaCe}_{0.7}\text{Zr}_{0.1}\text{Y}_{0.1}\text{Yb}_{0.1}\text{O}_3\$ \(BCZYYb\) Proton-Conducting Membranes](#)
Huayang Zhu, Sandrine Ricote, Chuancheng Duan et al.

Investigate your battery materials under defined force!
The new PAT-Cell-Force, especially suitable for solid-state electrolytes!



- Battery test cell for force adjustment and measurement, 0 to 1500 Newton (0-5.9 MPa at 18mm electrode diameter)
- Additional monitoring of gas pressure and temperature

www.el-cell.com +49 (0) 40 79012 737 sales@el-cell.com

EL-CELL[®]
electrochemical test equipment





Electrochemical Modeling of the Current-Voltage Characteristics of an SOFC in Fuel Cell and Electrolyzer Operation Modes

J.-C. Njodzefon,^{a,*} D. Klotz,^a A. Kromp,^a A. Weber,^a and E. Ivers-Tiffée^{a,b,**}

^aInstitut für Werkstoffe der Elektrotechnik (IWE), Karlsruher Institut für Technologie (KIT), D-76131 Karlsruhe, Germany

^bCenter for Functional Nanostructures (CFN), Karlsruher Institut für Technologie (KIT), D-76131 Karlsruhe, Germany

A zero-dimensional and isothermal stationary model demonstrably predicting the current-voltage (C/V) characteristic of an anode supported SOFC single cell is for the first time verified for C/V characteristics measured in electrolysis mode. The accuracy of the presented model was increased by including the actual cell temperature under current load, determined by an impedance-based temperature measurement routine. C/V characteristics measured at 800°C in the range from 0.66 V to 1.6 V for H₂O:H₂ compositions 70:30 and 30:70 reveal a pronounced asymmetric operation of the fuel electrode supported cell in electrolysis mode. This experimentally observed behavior is accurately reproduced by the model and is explained by (i) increasing polarization losses related to Knudsen diffusion and (ii) decreasing reaction rate in dry conditions at the fuel electrode at high current densities in electrolysis mode.

© 2013 The Electrochemical Society. [DOI: 10.1149/2.018304jes] All rights reserved.

Manuscript submitted November 5, 2012; revised manuscript received January 16, 2013. Published January 28, 2013. This was Paper 1517 presented at the Boston, Massachusetts, Meeting of the Society, October 9–14, 2011.

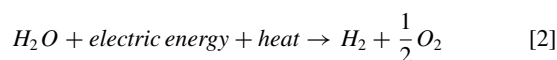
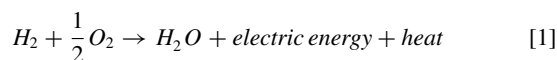
The adverse impact of conventional energy production methods like nuclear and fossil fuel combustion on the environment has led to increased exploitation of alternative but above all greener and more sustainable energy sources like wind and solar.

Energy from these renewable sources however is intermittent and would strain power grids. More so solar and wind parks are generally far off from the consumer, so that an important fraction of generated power is lost (dissipated) during transportation to consumer.

It therefore may be of good economic sense to temporarily store electrical energy from these renewable sources as hydrogen either to transport to consumer or feed to the grid with stable and controllable power through the fuel cell again.

A Solid Oxide Fuel Cell (SOFC), usually converting hydrogen (Fig. 1a) as well as hydrocarbon fuels directly into electricity (Eq. 1), has the ability to operate in a reverse mode as Solid Oxide Electrolysis Cell (SOEC). In this reverse or electrolysis mode (Eq. 2) hydrogen is produced by electrochemical reduction of steam using electrical (ΔG) and thermal ($T\Delta S$) energy (Fig. 1b).

In this way, the consumed electrical and thermal energy is “stored” as chemical energy in the products, thereby offering an important alternative to the portfolio of the till now not quite efficient electrical energy storage solutions. In this light wind and solar parks can potentially profit from electrolysis operation of an SOFC by having their surplus electricity at off-peak converted into hydrogen and stored, to then be reconverted to electricity with the same systems at peak load.



Recording the current/voltage (C/V) characteristic offers information about cell performance and if done at regular intervals also reveals performance degradation (aging). However, optimizing state-of-the-art SOFC for electrolysis or dual operation mode capability requires a profound understanding of the loss mechanisms taking place in the air electrode, the electrolyte, the fuel electrode and the substrate. This information cannot be gained from measurement of C/V curves alone. Physically motivated electrochemical models predicting the C/V curve require not only a thorough understanding of individual loss mechanisms but more importantly a means to quantitatively pre-

dict them. The area-specific resistances (ASRs) correlated with these loss processes are definitely functions of operating conditions, such as current load, temperature, gas mixture, fuel consumption, and so on.

Electrochemical impedance spectroscopy (EIS) and physically motivated equivalent circuit models (ECM) make it possible to quantify the ASRs and adequate variations of operating conditions enables determination of adequate model elements and parameters.¹ A comprehensive zero dimensional model predicting these ASRs and therefore the C/V-characteristic of fuel electrode supported cells in SOFC mode was for the first time presented in,² but is yet to be satisfactorily demonstrated for SOEC mode.

Udagawa et al.³ have developed a one dimensional dynamic model to study the steady state of a SOEC stack and in⁴ they investigate the dynamic behavior in an according model. Ni et al. in⁵ developed a theoretical model in which they simulated the C/V characteristic of a solid oxide steam electrolyzer. The effects of material properties and operation parameters on the C/V characteristic were investigated through parametric analysis. Model validation was done with experimental data from literature. Ni in⁶ further investigated the electrolysis of Carbon dioxide using a 1D and a 2D model, with the latter being a thermal fluid model consisting of a 1D and a Computational Fluid Dynamics (CFD) model. This is not uncommon in literature as a handful of CFD or multi-physic models have been used to model or investigate fluid, heat and mass transfer in SOEC.^{7–9} Quite instructive is the 2D model recently presented by Ni¹⁰ for the co-electrolysis of steam and carbon dioxide in which a third sub model describing the reversible water gas shift and reversible methanation reactions is included. Clearly very few stand-alone mathematical or electrochemical zero dimensional SOEC models reproducing the C/V-characteristic are available in literature.

Leonide et al. have recently introduced and experimentally verified a zero dimensional and isothermal electrochemical model² that predicts the C/V characteristic of well characterized^{1,11} fuel electrode supported single cells for SOFC operation. For the first time, this isothermal stationary model is applied for SOEC operation and some of the consequential findings are discussed in this contribution. The origin of asymmetric C/V curves in SOFC and SOEC operation will be explained and an even better accuracy of our model is achieved by including the actual cell temperature determined through an impedance-based temperature measurement routine. As the model provides quantitative information about the different losses in the cathode, the electrolyte, the anode and the substrate for any operating condition, it is applicable to understand the electrochemical behavior of a cell, to determine appropriate operating conditions and to optimize the cell performance with respect to the operating conditions in a system.

*Electrochemical Society Student Member.

**Electrochemical Society Active Member.

^zE-mail: jean-claude.njodzefon@kit.edu

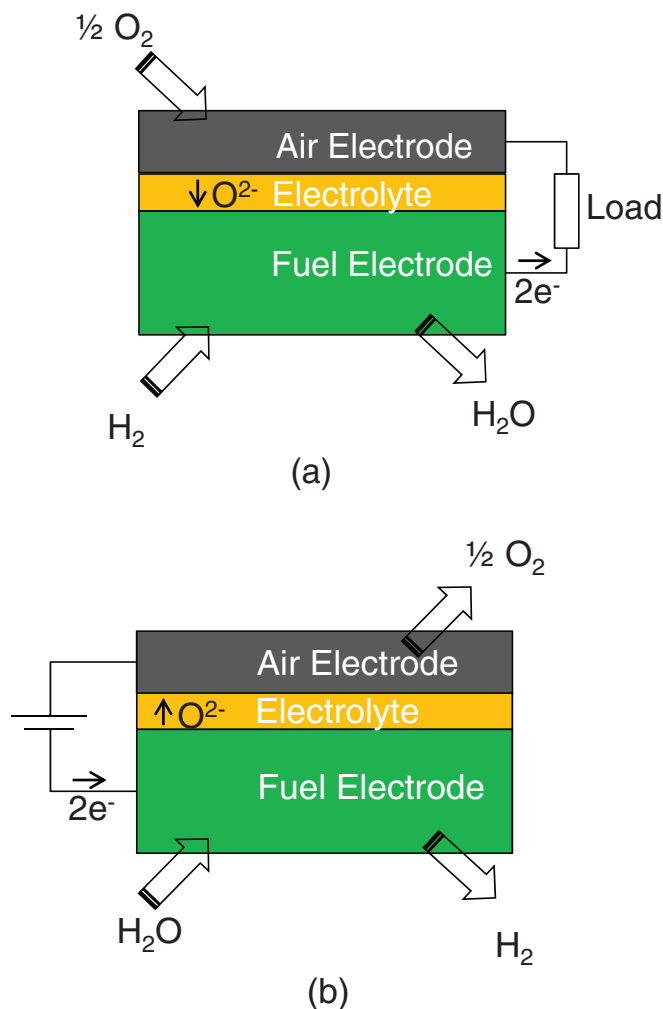


Figure 1. (a) SOFC and (b) SOEC operation modes.

Model Presentation

In Ref. 2 the C/V characteristics of the same fuel electrode supported SOFC single cell used in the actual measurements were modeled based on fundamental electrochemical and physical relationships, such as the Butler-Volmer (BV) equation, Fick's law and Ohm's law, yet without any further simplifications. Our zero-dimensional and isothermal stationary model is implemented in *Matlab*, taking into consideration the following issues:

- the use of generally valid approaches, derived from physically well-founded equations or experimentally validated empirical equations (power law ansatz),
- all model parameters were determined from open-circuit impedance measurements (with the exception of the charge transfer coefficients α_{an} and α_{cat} that were determined from impedance measurements under load),
- all processes contributing to the internal resistance of the cell are taken into consideration in the model:
 - ohmic losses in the electrolyte and the electrodes
 - gas diffusion (or concentration) overpotential in the substrate and the fuel electrode and the air electrode
 - activation polarization at the fuel electrode and the air electrode.

In the following subsections, the modeling equations and the identified model parameters are completely introduced.

Operating voltage.— The cell or operating voltage (U_{cell}) is calculated by subtracting the individual overvoltages from the open-circuit

voltage U_{OCV} (sticking to SOFC operation mode nomenclature, fuel electrode quantities are subscripted with “an” while those referring to the air electrode subscripted with “cat”):

$$U_{cell} = U_{OCV} - (\eta_{ohm} + \eta_{act,an} + \eta_{act,cat} + \eta_{conc,an} + \eta_{conc,cat}) \quad [3]$$

η_{ohm} denotes the overpotential owing to ohmic losses in the cell, $\eta_{act,an}$, $\eta_{act,cat}$, $\eta_{conc,an}$, and $\eta_{conc,cat}$ denote the activation and concentration overpotentials at the fuel and air electrodes respectively.

Open-circuit voltage.— The open-circuit voltage U_{OCV} is described by the Nernst equation adapted for H_2/H_2O operation:

$$U_{OCV}(T) = U_0(T) - \frac{RT}{2F} \ln \left(\frac{p_{H_2} O_{an}}{p_{H_2,an} \cdot \sqrt{p_{O_2,cat}}} \right) \quad [4]$$

In Eq. 4, $U_0(T)$ is the theoretical standard voltage,¹² $pX_{an/cat}$ the partial pressure of gas X at fuel electrode (“an”) and air electrode (“cat”), respectively, in atm normed to the absolute pressure of 1 atm. Meanwhile R , F and T represent universal gas constant, Faraday constant and absolute temperature, respectively.

Ohmic losses.— Ohmic losses occur during electronic and/or ionic transport through the electrodes and the electrolyte. The overall ohmic losses are the sum of each individual ohmic contribution. According to Ohm's law, the ohmic overpotential increases linearly with the current density j .

$$\eta_{ohm} = j \cdot \sum_k R_k = j \cdot R_{ohm} \quad [5]$$

R_k is the area-specific ohmic resistance with contributions of substrate, fuel electrode, electrolyte, interdiffusion layer, GDC interlayer and air electrode respectively. As the conductivities of the substrate, the fuel electrode and the air electrode are orders of magnitude higher, R_{ohm} is dominated by the ohmic resistance of the YSZ electrolyte, the GDC interlayer and the interdiffusion zone between them.¹³ This was proven by thorough microstructural and electrical analysis of the tested fuel electrode supported cell.^{1,11} Therefore it can be modeled by thermally activated charge transport mechanisms with the following relationship, derived from the Arrhenius Equation:^{14,15}

$$R_{ohm}(T) = \frac{T}{B_{ohm}} \exp \left(\frac{E_{act,ohm}}{RT} \right) \quad [6]$$

$E_{act,ohm}$ represents the activation energy in kJ/mol, whereas B_{ohm} is a material-specific constant. It should be taken into account that these values do not represent physically meaningful material parameters of the individual layers. In our model we are using averaged values representing the thermally activated ionic conduction of the two layers and the interdiffusion zone in between. This approach enables a precise simulation of the ohmic losses in any CV-characteristic for the given cell but is unsuitable to predict the performance for a variation in layer thicknesses or microstructure features as porosity.

Diffusion overpotential.— The gas diffusion (or concentration) polarization is caused by the partial pressure difference between the gas channel atmosphere and the three-phase boundary (TPB), acting as the driving force for the diffusion of reactants and reaction products in the porous electrodes and the substrate. The corresponding overpotential ($\eta_{conc,e}$) is calculated via the Nernst equation (Eq. 4), from which the following Eqs. 7 and 8 can easily be derived:¹⁶

$$\eta_{conc,an} = \frac{RT}{2F} \ln \left(\frac{p_{H_2} O_{an}^{TPB} \cdot p_{H_2,an}}{p_{H_2} O_{an} \cdot p_{H_2,an}^{TPB}} \right) \quad [7]$$

$$\eta_{conc,cat} = \frac{RT}{4F} \ln \left(\frac{p_{O_2,cat}}{p_{O_2,cat}^{TPB}} \right) \quad [8]$$

$p_{H_2,an}$, $p_{H_2O,an}$, and $p_{O_2,cat}$ are the known partial pressures of hydrogen, water and oxygen, respectively, in the gas channel.

As shown in Ref. 17 the unknown partial pressures $pH_{2,an}^{TPB}$, $pH_2O_{an}^{TPB}$, and $pO_{2,cat}^{TPB}$ are determined by applying Fick's first law and assuming a linear concentration gradient as a function of the current density j :

$$pH_{2,an}^{TPB} = pH_{2,an} - \frac{RTL_{an}}{2FD_{H_2}^{eff}P_0} \cdot j, \quad [9]$$

$$pH_2O_{an}^{TPB} = pH_2O_{an} + \frac{RTL_{an}}{2FD_{H_2O}^{eff}P_0} \cdot j \quad [10]$$

and

$$pO_{2,cat}^{TPB} = pO_{2,cat} - \left(\frac{p_{tot} - pO_{2,cat}}{p_{tot}} \right) \frac{RTL_{cat}}{4FD_{O_2}^{eff}P_0} \cdot j \quad [11]$$

p_{tot} denotes the absolute atmospheric pressure (1 atm), and $P_0 = 1.0133 \cdot 10^5$ Pa/atm denotes the conversion factor from atm to Pa. By inserting Eqs. 9, 10, and 11 into Eqs. 7 and 8, Eqs. 12 and 13 are obtained, which relate the diffusion-based voltage drop $\eta_{conc,el}$ to the current density j :¹⁷

$$\eta_{conc,an} = \frac{RT}{2F} \ln \left(\frac{1 + \frac{RTL_{an}}{2FD_{H_2O}^{eff}pH_2O_{an}P_0} \cdot j}{1 - \frac{RTL_{an}}{2FD_{H_2}^{eff}pH_{2,an}P_0} \cdot j} \right) \quad [12]$$

$$\eta_{conc,cat} = \frac{RT}{4F} \ln \left(1 / \left(1 - \frac{RTL_{cat}(1 - pO_{2,cat}/p_{tot})}{4FD_{O_2}^{eff}pO_{2,cat}P_0} \cdot j \right) \right) \quad [13]$$

L_{an} and L_{cat} denote the thickness of the fuel electrode substrate (here: 1 mm) and the thickness of the air electrode (here: 45 μ m). D_i^{eff} is the only unknown parameter in these equations. It is the effective molecular diffusion coefficient, which can also be expressed as:¹⁷

$$D_i^{eff} = \psi_{el} \cdot D_{mol,i}, \quad [14]$$

with

$$\psi_{el} = \frac{\varepsilon_{el}}{\tau_{el}}, \quad [15]$$

and

$$\frac{1}{D_{mol,i}} = \frac{1}{D_{bulk,i}} + \frac{1}{D_{Knudsen,i}}. \quad [16]$$

ψ_{an} and ψ_{cat} are the structural parameters of the fuel and air electrodes respectively, that describe the relationship between volumetric porosity ε_{el} and tortuosity τ_{el} of the corresponding electrode microstructure. A detailed description and the procedure to obtain these parameters are discussed elsewhere.² The molecular diffusion coefficients $D_{mol,i}$ of the single components are composed of the Knudsen diffusion coefficient $D_{Knudsen,i}$ and the bulk diffusion coefficient $D_{bulk,i,j}$ (Eq. 16).¹⁷⁻²⁰ $D_{Knudsen,i}$ can be calculated using Eq. 17²¹ and must be considered for structures with pore sizes in the order of the mean free path length of the diffusing particles. The binary diffusion coefficient $D_{bulk,i,j}$ which is used in general for diffusion processes in the gas atmosphere, can be estimated for binary gas mixtures according to the Chapman-Enskog theory^{17,22} (cf. Eq. 18).

$$D_{Knudsen,i} = \frac{2}{3} \cdot r_{Por,el} \sqrt{\frac{8RT}{\pi M_i}} \quad [17]$$

$$D_{bulk,i,j} = \frac{1.86 \cdot 10^{-3} \cdot T^{1.5} \sqrt{M_i^{-1} + M_j^{-1}}}{p_{tot} \cdot \sigma_{ij}^2 \cdot \Omega_D} \quad [18]$$

with the collision integral

$$\Omega_D = \frac{A}{\tau_{ij}^B} + \frac{C}{\exp(D \cdot \tau_{ij})} + \frac{E}{\exp(F \cdot \tau_{ij})} + \frac{G}{\exp(H \cdot \tau_{ij})}, \quad [19]$$

whereby

$$\tau_{ij} = \frac{k \cdot T}{\sqrt{\varepsilon_i \cdot \varepsilon_j}} \quad [20]$$

and the average collision diameter

$$\sigma_{ij} = \frac{\sigma_i + \sigma_j}{2}. \quad [21]$$

The molar mass M_i , characteristic length σ_i , characteristic Lennard-Jones energy ε_i of gas species i (given as ratio with Boltzmann constant k , i.e. ε_i/k) as well as the coefficients $A-H$ that appear in Eqs. 17-21 are obtained from Ref. 23 and summarized in Table II. The constants $r_{Por,el}$, which denote the mean pore radius of each electrode structure (index "el"), were extracted from semi-quantitative image analysis of SEM micrographs of the according electrode structures. The mean pore radius of the substrate was estimated to be $r_{Por,an} = 600$ nm and that of the air electrode to be $r_{Por,cat} = 600$ nm.² Since for these pore radii, the Knudsen diffusion coefficients and the bulk diffusion coefficients are in the same order of magnitude, Knudsen diffusion had to be considered as well.

As the diffusion (or concentration) overvoltage is simulated based on general physical equations and properties (porosity, pore size, tortuosity, thickness) of the porous layers the model is able to predict the impact of variations of these properties on the CV-characteristic. It should be noted here that the gas diffusion in the electrochemically active part of the fuel and air electrode close to the electrolyte, which is strongly coupled with the electrochemical reactions and the ionic transport, is not considered in the diffusion overpotential.²⁴⁻²⁶

Activation overvoltage.— Activation polarization describes the electrochemical loss mechanisms taking place mainly at the three-phase boundary (TPB) where ionic-conducting, electronic-conducting and gas phases meet. In most models^{27,28} the activation polarization is calculated separately for fuel electrode and air electrode, in both cases using the BV equation:

$$j = j_{0,el} \left[\exp \left(\alpha_{el} \frac{n_e F \eta_{act,el}}{RT} \right) - \exp \left(-(1 - \alpha_{el}) \frac{n_e F \eta_{act,el}}{RT} \right) \right]. \quad [22]$$

The use of the full BV equation to model the activation overpotential of fuel and air electrodes in SOFC (and SOEC) operation is not completely free of controversy. This is because the BV equation in its natural form is defined for a single step single electron transfer reaction whereas the reactions in Eq. 1 and 2 involve the overall transfer of multiple electrons in a multistep process in each electrode. Furthermore, the rate determining step is not always known and even if known cannot be guaranteed to be the same over the entire operation range. However, we introduced the experimentally determined *transfer coefficient* α instead of the *symmetry factor* β in the BV equation, as discussed to be reasonable by Noren et al.,²⁹ Mann et al.³⁰ but most importantly by Bockris et al.³¹ Their reasoning was included in our model approach and should weaken severity of criticism. We acknowledge, that C/V curves in SOC mode show mostly linear behavior for small current densities.^{32,33} However, we prefer the BV here because of the following reasons: (i) neither the Tafel nor the linear approach are able to represent the electrode characteristics accurately over such a wide operation range as discussed here (current density up to ± 2.5 A/cm², $pO_{2,cat}$ from 0.21 to 0.01 atm, pH_2O_{an} from 0.2 to 0.8 atm). This aspect is taken seriously and treated in more detail in the results and discussion section., (ii) the BV is favored for SOCs by a serious number of authors^{3,5,18,21,27,28} and, (iii) a widely agreed alternative to BV is not generally known, nor demonstrated on measurements spreading over a wide operation range. Furthermore, a "linear" activation approach^{34,35} based on the exchange current density using the power law ansatz fails, because it will end up in nonlinear behavior if the partial pressures at the TPB are taken into consideration.

It is well known to the authors, that complex homogenized or even space resolved electrode models for cermet anodes and mixed

ionic-electronic conducting cathodes are available,^{26,36–41} which are capable of describing the Ni/8YSZ fuel electrode and the LSCF air electrode applied here. These models employ coupled nonlinear elementary kinetic reactions, that could substitute the BV approach. However, it is questionable, if these models are already applicable to “real” electrode structures. Various material and microstructural parameters are required, such as bulk and surface properties of electrodes.^{40–42} Their electrochemical features were already evaluated on model electrodes.^{43–46} Unfortunately, these values depend on raw material, sample processing and impurities,^{42–44} and are responsible for discrepancies of one order of magnitude and more.^{45,46} One alternative is fitting some of the model parameters to experimental results,³⁸ but this limits the applicability of the model to the experimentally evaluated operation range.

For good reasons, we prefer a much simpler approach, assuming that the electrochemistry at air electrode and fuel electrode is governed by one BV-type reaction each.

Here, $j_{0,el}$ is the partial pressure and temperature dependent exchange current density of the fuel electrode or air electrode, n_e the number of exchanged electrons, which is in our case $n_e = 2$, α_{el} the apparent charge transfer coefficient, and $\eta_{act,el}$ the activation overpotential of the according electrode. The charge transfer coefficient α_{el} is an indicator of the symmetry of the activation energy barrier when a positive or negative overpotential is applied.⁴⁷

The exchange current densities $j_{0,el}$ obey the semi-empirical Eqs. 23 and 24.

$$j_{0,an} = \gamma_{an} (pH_{2,an}^{TPB})^a (pH_2O_{an}^{TPB})^b \exp\left(-\frac{E_{act,an}}{RT}\right) \quad [23]$$

$$j_{0,cat} = \gamma_{cat} (pO_{2,cat}^{TPB})^m \exp\left(-\frac{E_{act,cat}}{RT}\right) \quad [24]$$

It is worth mentioning that the partial pressures in Eqs. 23 and 24 are those at the three-phase boundary. They can be calculated with the known quantities of the partial pressures in the gas channels and the diffusion overvoltage with Eqs. 9 to 11. The charge transfer coefficient α_{el} , the prefactors γ_{an} and γ_{cat} , the exponents a , b , and m as well as the activation energies $E_{act,an}$ and $E_{act,cat}$ are also given in Ref. 2.

Table 1 lists the values of all the parameters used in this work. They are taken from Ref. 2, where they were determined by extensive impedance analysis for an identical fuel electrode supported cell type (c.f., Experimental). If this cell type is modified in layer thicknesses or microstructure, these parameters need to be justified by a brief impedance analysis routine. However, if cell types deviate clearly in composition (e.g., (La,Sr)MnO₃/YSZ air electrode) or cell design (e.g., metal supported cell), appropriate equivalent circuit models have to be developed first, and then used to quantify the area specific resistance of individual polarization mechanisms.

TABLE I. System specific modeling parameters used in this work determined via EIS for the same type of fuel electrode supported single cells as investigated herein (Ref. 2).

Parameter	Value/Expression	Unit
B_{ohm}	$4.1879 \cdot 10^{12}$	S · K/m ²
$E_{act,ohm}$	90.31	kJ/mol
a	−0.10	—
b	0.33	—
m	0.22	—
γ_{an}	$1.82527 \cdot 10^6 \cdot T$	A/m ²
γ_{cat}	$1.51556 \cdot 10^8 \cdot T$	A/m ²
$E_{act,an}$	105.04	kJ/mol
$E_{act,cat}$	139.86	kJ/mol
α_{an}	0.59	—
α_{cat}	0.65	—
ψ_{an}	0.13	—
ψ_{cat}	0.09	—

TABLE II. General physical modeling parameters and constants from literature (Ref. 23) used in this work.

Parameter	Value/Expression	Unit
R	8.3145	J/molK
F	96485.34	C/mol
M_{H_2}	0.002016	kg/mol
M_{H_2O}	0.018015	kg/mol
M_{N_2}	0.028013	kg/mol
σ_{H_2O}	2.641	Å
σ_{H_2}	2.827	Å
σ_{N_2}	3.798	Å
σ_{O_2}	3.467	Å
ε_{H_2}/k	59.7	K
ε_{H_2O}/k	809.1	K
ε_{N_2}/k	71.4	K
ε_{O_2}/k	106.7	K
A	1.06036	—
B	0.15610	—
C	0.19300	—
D	0.47635	—
E	1.03587	—
F	1.52996	—
G	1.76474	—
H	3.89411	—

Experimental

Cell system.— The investigations were performed on state of the art anode supported cells manufactured by Forschungszentrum Jülich, one of the best-performing, most stable and hence most investigated ASC available.^{48,49} Our group performs extensive EIS analysis on ASCs since more than 10 years^{50,51} and developed a well-proven equivalent circuit model (ECM) representing the impedance response of the ASC type used herein.^{1,11} In the ECM, each electrochemical process is represented by a single equivalent circuit element. Complex Nonlinear Least Squares (CNLS)-fit of the ECM to measured impedance spectra facilitate a separated, quantitative analysis of the individual electrochemical loss processes at fuel electrode and air electrode. The cells (Fig. 2a, 2b) were built on a 1000 μm Ni/8YSZ substrate, followed by a fuel electrode functional layer (Ni/8YSZ, thickness 7 μm) and the electrolyte (8YSZ, thickness 10 μm). Onto the electrolyte, a GDC interlayer (Ce_{0.8}Gd_{0.2}O_{2–δ}) with a thickness of 7 μm was screen-printed and fired. This GDC interlayer serves to prevent chemical reaction between the electrolyte material 8YSZ and the air electrode material LSCF (La_{0.58}Sr_{0.4}Co_{0.2}Fe_{0.8}O_{3–δ}, thickness 45 μm), screen-printed on top of the fired GDC layer. The active surface area of the air electrode, and therefore the active cross-sectional area of the cell, is 1 cm² (10 mm × 10 mm).

Additionally, an OCV probe before and after the air electrode in direction of the gas flow monitors the open-circuit voltage U_{OCV} . The fuel electrode substrate has a cross-sectional area of 50 mm × 50 mm and is entirely covered by the thin-film electrolyte.

C/V measurements.— The model predictions of C/V curves were validated with C/V measurements recorded for three different gas mixtures at the fuel electrode (H₂O:H₂: (a) 70:30, (b) 50:50, and (c) 30:70) at 800°C and one gas mixture (H₂O:H₂: 50:50) at 850°C. Air (N₂:O₂: 80:20) was used as oxidant gas in all experiments. The gas flow rate was kept constant for both electrodes at 250 sccm for all measurements shown here. The C/V curves were first measured in SOFC operation mode from 0 to 2.5 A/cm² or to a minimum cell voltage of 0.66 V. The voltage limit of 0.66 V was chosen to prevent alteration of the cell, i.e., oxidation of Ni to NiO and other irreversible reactions. After this measurement a waiting time of two hours at OCV was inserted so that the cell temperature could relax back to the set temperature. The C/V curve in SOEC mode was then recorded, from 0 to −2.5 A/cm² or until cell voltage exceeded 1.6 V. In both cases, no

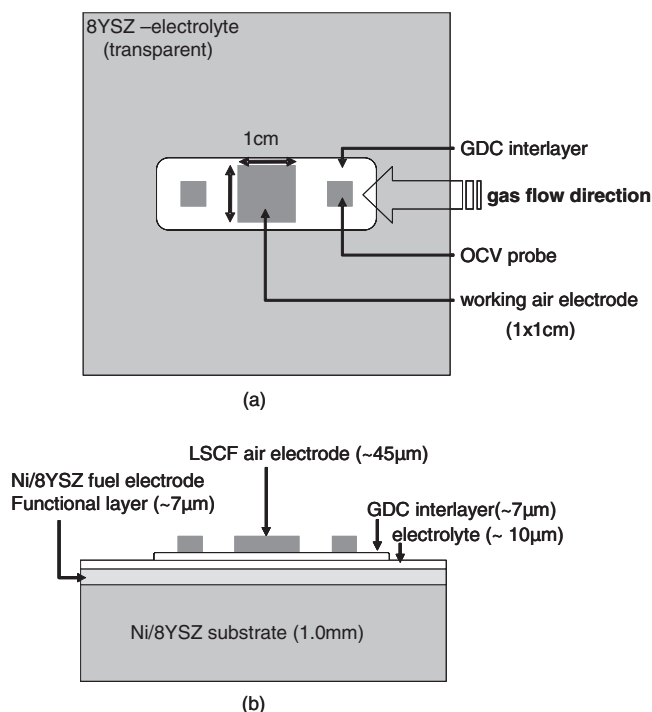


Figure 2. (a) Design of the working electrode and OCV probes at the air side of a fuel electrode supported SOFC single cell (top view). (b) Side view of the cell with the porous fuel electrode, the fuel electrode functional layer, the dense electrolyte, the GDC interlayer and the porous air electrode.

return sweeps were recorded to check for hysteresis. The applicability of the BV-equation was checked by further C/V curves recorded for the SOFC mode alone at the temperatures 750-, 700-, 650- and 600°C at a fuel electrode $\text{H}_2\text{O}:\text{H}_2$ ratio of 62:38.

C/V curve recording was done with an Agilent 6612C DC power supply. The current density was incremented by 0.02 A/cm^2 every 10 s. For the sake of clarity only every 10th measured data point is plotted in the C/V curves to validate model accuracy.

Results and Discussion

Validation of the model.— The first aim of this work was to test the applicability of our model, which was initially developed only for the SOFC mode, for the first time in SOEC mode. Figure 3 shows the C/V curves measured at 800°C as well as the corresponding simulation results for the $\text{H}_2\text{O}:\text{H}_2$ -ratios of 70:30, 50:50 and 30:70. Furthermore,

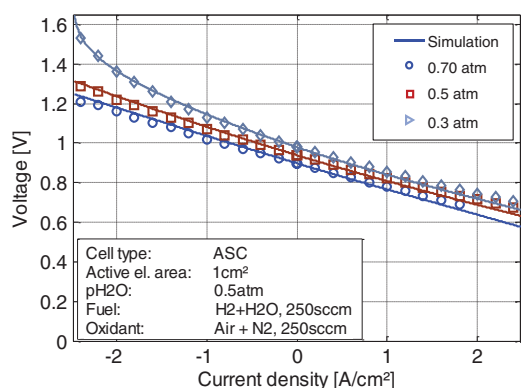


Figure 3. Simulation results of C/V curves at 800°C in SOFC and SOEC operation modes for fuel electrode $\text{H}_2\text{O}:\text{H}_2$ compositions 70:30, 50:50 and 30:70.

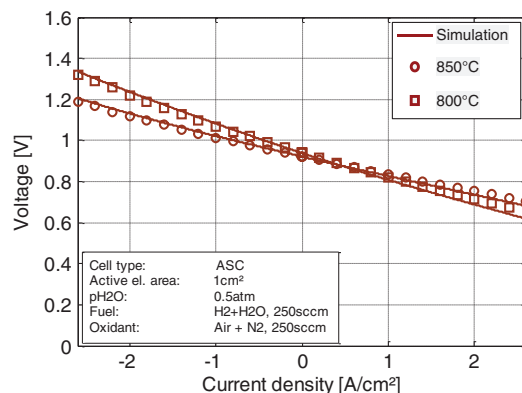


Figure 4. Simulation results of C/V curves at 800 and 850°C in SOFC and SOEC operation modes for fuel electrode $\text{H}_2\text{O}:\text{H}_2$ composition of 50:50.

Fig. 4 shows the C/V curves measured at 800 and 850°C at a gas composition of $\text{H}_2\text{O}:\text{H}_2 = 50:50$ and the related simulation results. All in all, the measured C/V curves are well reproduced by the model in both operation modes and for all gas compositions and temperature variations.

The accuracy of the model was estimated by analyzing the deviation between measurement and simulation, and the resulting absolute and relative¹ error curves for the 50:50 gas compositions at 800°C are displayed in Fig. 5a and 5b. First of all, the evolution of the error shows a characteristic difference between SOFC and SOEC mode. Whereas the error increases linearly in SOFC mode to 28 mV or 4.5% at 2.5 A/cm^2 , the error follows a semicircle in SOEC mode, with a maximum of 15 mV or 1.5% at -1.5 A/cm^2 . The error in SOEC mode seems to be caused by specific temperature effects originating from hydrogen generation consuming electrical (ΔG) and thermal ($T\Delta S$) energy in SOEC mode and by the generation of heat in SOFC mode. In order to analyze this the actual cell temperature in the reaction zone was determined through an impedance-based temperature measurement routine, first introduced in^{52,53} and described briefly in the next section.

Impedance-based temperature measurement.— The temperature around (and inside) a fuel electrode supported single cell is adequately measured by a nearby located thermocouple under open circuit conditions. In this case, the cell itself is in thermal equilibrium and no heat source or heat sink is present. However, a direct current gives rise to losses and the cell temperature cannot be further assumed constant. As thermocouples cannot be placed inside the cell, this problem has to be solved in a different way. In this case, the actual cell temperature is determined through an impedance-based temperature measurement routine. It is of common knowledge, that cell characteristics like the ohmic resistance R_0 depends on the local cell temperature. R_0 is defined as the intersection of the impedance curve with the real axis at high frequencies. Therefore, R_0 can be measured in a frequency range $> 300 \text{ kHz}$, where electrochemical loss processes causing an imaginary part in the impedance have already decayed. Hence, the impedance at $> 300 \text{ kHz}$ is exclusively ohmic. A change in this ohmic fraction is caused by the temperature dependency of the electrolyte conductivity that is of Arrhenius type.

However, the actual cell temperature cannot be determined exactly by simply measuring the ohmic fraction of the impedance spectrum of this particular cell, due to remaining uncertainties such as accurate electrolyte conductivity and thickness, and the residual ohmic resistance of the other cell components. Furthermore, it is a challenge to extract R_0 online from impedance data measured at 800°C be-

¹ Difference between measurement and simulation normalized with the dynamic range (maximum measured voltage in SOEC mode minus minimum measured voltage in SOFC mode)

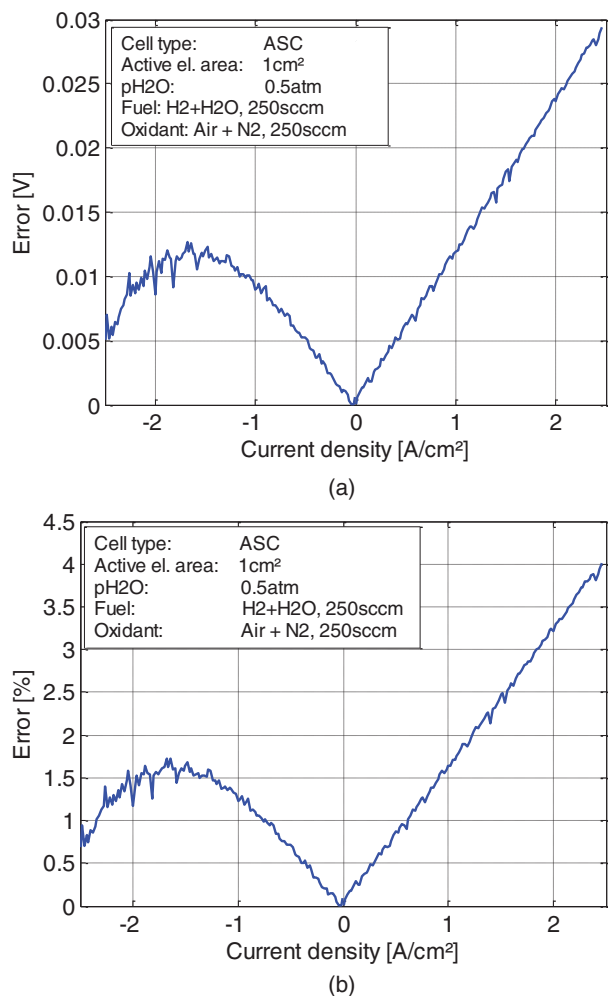


Figure 5. Error of the 800°C and 50:50 H₂O:H₂ fuel electrode gas mixture simulation (a) absolute value (b) relative value normalized with the dynamic range (maximum measured voltage in SOEC mode minus minimum measured voltage in SOFC mode).

cause of high frequencies (>300 kHz) and low impedance values ($|Z| < 100$ mΩ).

The concept presented here is to measure the real part of the impedance at only one given frequency, $\text{Re}(Z(f_T))$, for both a reference curve at different temperatures and OCV and a load curve of the same fuel electrode supported cell. This works well when the frequency for $\text{Re}(Z(f_T))$ is (i) high enough to avoid influences from polarization processes and (ii) low enough to enable consistent measurement results. It can be seen from the parallel shift of the real part of the impedance, as demonstrated in Fig. 6 for different current densities, that the frequency range between $100 \text{ kHz} \leq f \leq 200 \text{ kHz}$

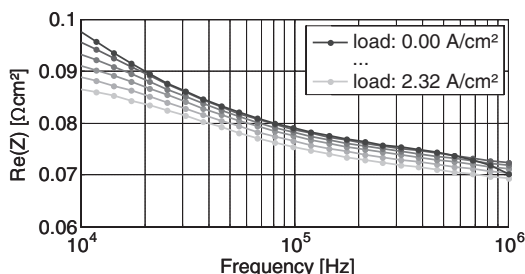


Figure 6. Real part of impedance spectra against frequency for different current densities.

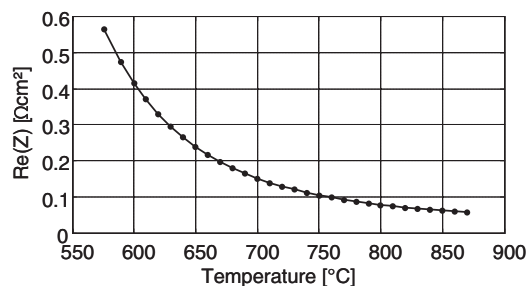


Figure 7. Reference curve for the impedance-based temperature measurement routine at OCV at different furnace temperatures.

is suitable for $\text{Re}(Z(f_T))$. The characteristic shape of the impedance curves does not change at these high frequencies but is vertically shifted. This vertical shift is attributed to the electrolyte resistance, which only depends on temperature, and the variation thereof is exclusively caused by the applied current. It is completely out of question, that the applied current affects a polarization process. The real part of the impedance does not converge to the ohmic resistance due to polarization effects of the grain boundaries in the electrolyte.⁵⁴ The imaginary part of the impedance is slightly affected by the inductivity in the test setup, which can be assumed to be purely imaginary ($Z_L = j\omega L$). It should be noted that in addition to the high frequencies and very low impedance values as mentioned above, also an offset current density of up to 2.3 A/cm² had to be applied. Because of the typically flat impedance spectra also the signal to noise ratio of the imaginary part is worse. Therefore the imaginary part of the impedance measurements does not add further information for the temperature measurement proposed here and is not shown.

The frequency chosen here was $f_T = 120$ kHz and the temperature change of the cell under current load was calculated then by the following method:

1. Determining $\text{Re}(Z(f_T))$ for different furnace temperatures at OCV and thus establishing a reference curve for a particular cell without internal heat production. An example for such a reference curve at OCV is shown in Fig. 7.
2. Measuring $\text{Re}(Z(f_T))$ under various (stepwise increasing) constant loads at one fixed furnace temperature (load curve).

The actual temperature of the cell can then be determined more exactly by using the inverse function of the reference curve at OCV, as demonstrated in Fig. 8. In fact, this method determines the temperature of the electrolyte, which is adjacent to the reaction zone producing either hydrogen in electrolysis mode or consuming hydrogen in fuel cell mode. Compared to the thermocouple located in the gas channel and thus in a distance of 1.5 mm above the cell, the electrolyte applied as a resistive temperature sensor provides more accurate information about the cell temperature. In Fig. 9 this so-called actual cell temperature and the thermocouple temperature are plotted against the applied current density. Obviously, the actual cell temperature rises with current density

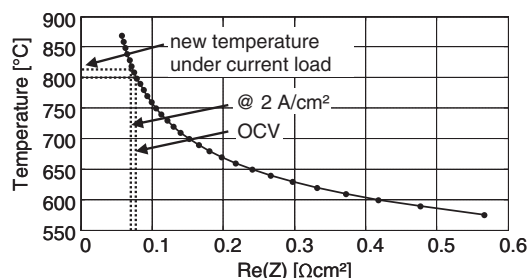


Figure 8. Determination of the electrolyte or real cell temperature under current load from the inverse reference curve.

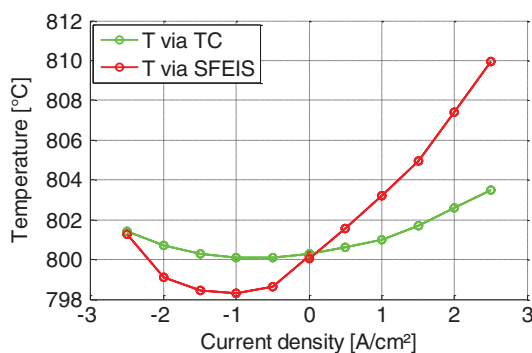


Figure 9. Cell temperature as a function of current density during SOFC and SOEC operation modes at 800°C and H₂:H₂O ratio of 50:50.

more in SOFC than in SOEC mode. This is easily explained by the fact, that heat is consumed during hydrogen production in electrolysis mode. Therefore, an important share of the observed deviations in C/V- curves between SOFC and SOEC mode are caused by temperature effects as our model is assumed isothermal. With the revised temperature-dependent model, which includes the actual cell temperature, the accuracy of simulation is improved particularly for SOFC mode. At a current density of +2.4 A/cm² the error decreases from 28 mV (4.5%) in Figs. 5a, 5b to 18 mV (2.5%) in Figs. 10a, 10b. The SOEC curve which witnessed a maximum temperature change of only 2°C (at $j = -1$ A/cm²) seems to be insensitive to the temperature correction function. With a maximum attained accuracy of 2.5% in SOFC mode, these results suggest that the temperature correction functions improve accuracy to around 2.5% and that the SOEC does not require any temperature correction in the investigated current density range.

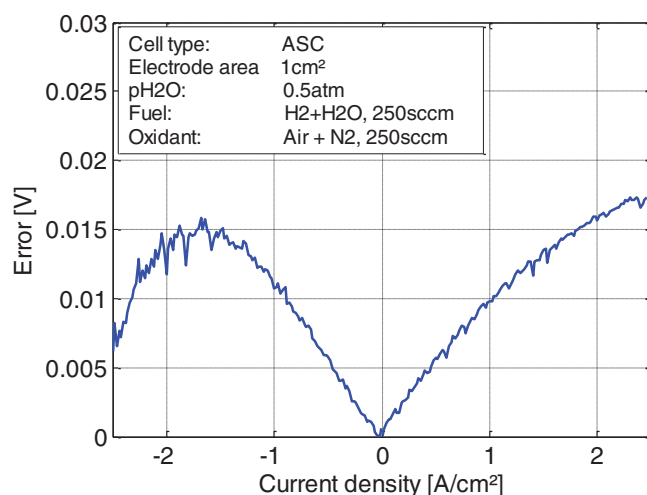
Interesting enough, the trends of the error curves are now similar to the temperature trends in the respective operation modes. We suggest that the still remaining uncorrected error (or the model inaccuracy) is either related (i) to an intrinsic temperature dependent characteristic not described by our model, or (ii) to a summation of residual temperature dependent inaccuracies in already described characteristics. More details of the impedance-based temperature measurement routine were first reported in Ref. 52.

Statements of achieved modeling accuracy.— The now obtained model accuracy for predicting the C/V-characteristics in SOFC and SOEC mode allows the following statements:

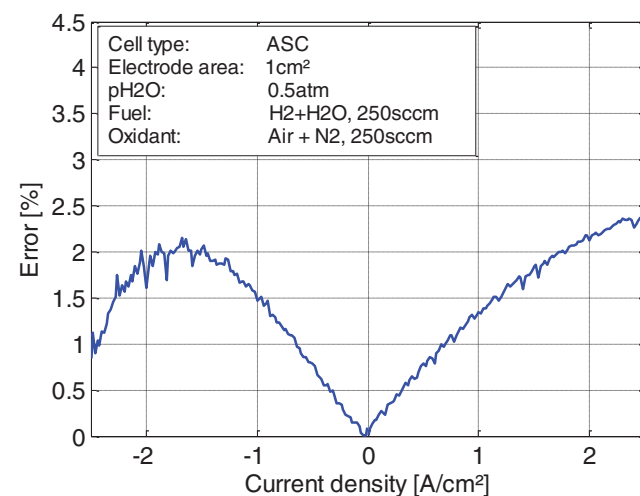
1. It depicts a thorough understanding of cell kinetics. The area specific resistances of the individual polarization mechanisms at any given operation point are well predictable, e.g., (i) the electrolyte resistance at any given temperature, (ii) the individual area specific resistance of both electrodes at any temperature and gas composition, (iii) the individual reaction rates (or exchange current densities) at both electrodes under any given operating condition, (iv) the gas diffusion related area specific resistance of both electrodes. This comprehensive knowledge allows explaining the asymmetry in the C/V characteristics among SOFC and SOEC mode.
2. The model and its appreciable results are qualified for a further discussion about the adequacy of the BV approach.
3. The model is supportive in predicting (i) the operating conditions for efficient SOC operation of fuel electrode supported cells and stacks, and (ii) the required cell component improvements for enhancing performance at any given operation point.

These three points are discussed in the following subsections in detail.

Asymmetry of the C/V characteristics.—Alongside validating this zero-dimensional stationary model for SOEC mode, another concern was to propose an explanation for the asymmetry best observable for the C/V characteristics at $p_{\text{H}_2\text{O}} = 0.7$ atm (SOFC-mode) and $p_{\text{H}_2\text{O}}$



(a)



(b)

Figure 10. Error of the 800°C and 50:50 H₂O:H₂ fuel electrode gas mixture simulation with real cell temperature determined through SF-EIS (a) absolute value (b) relative value normalized with the dynamic range (maximum measured voltage in SOEC mode minus minimum measured voltage in SOFC mode).

= 0.3 atm (SOEC-mode) in Fig. 3. These operating conditions describe a scenario, in which the fraction of the gas, which is consumed in the electrochemical reaction, is 30% at zero current conditions and therefore subject to depletion at current densities increasing to 2.5 A/cm² in SOFC mode and to −3 A/cm² in SOEC mode. In order to understand this phenomena, a closer look at the calculated individual overvoltages for these gas compositions needed to be taken.

The resulting curves for the individual overpotentials are shown in Fig. 11a and 11b. In these figures a depletion of gas occurs at each half of the corresponding figure. Naturally, the overvoltage originating from the ohmic resistance, η_{ohm} , is symmetrical in both modes. For SOFC mode, all overpotentials displayed in Fig. 11a increase rather linearly and gas diffusion of the air electrode, $\eta_{\text{conc,cat}}$, contributes the least. At 2.4 A/cm², the contributions of gas diffusion and activation overpotential of the fuel electrode, $\eta_{\text{conc,an}}$ and $\eta_{\text{act,an}}$ and activation overpotential of the air electrode, $\eta_{\text{act,cat}}$, are of similar size. After this point the magnitude of $\eta_{\text{conc,an}}$ starts to dominate the other two polarization losses.

For SOEC mode, and from all overpotentials displayed in Fig. 11b, only gas diffusion and activation overpotential of the air electrode, $\eta_{\text{conc,cat}}$ and $\eta_{\text{act,cat}}$, increase rather linearly up to −2.4 A/cm²

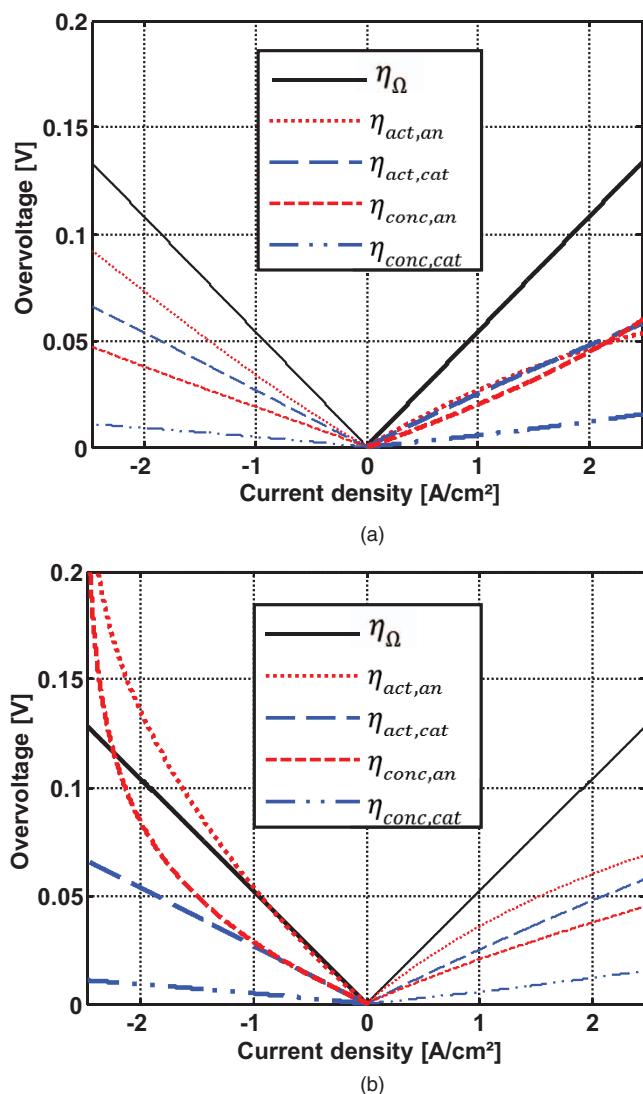


Figure 11. Overvoltages of curves simulated at 800°C for (a): 70:30 and (b) 30:70 fuel electrode H₂O:H₂ gas composition.

and contribute least to the total polarization loss. In contrast to this, gas diffusion and activation overpotential of the fuel electrode, $\eta_{\text{conc,an}}$ and $\eta_{\text{act,an}}$, drastically increase at high current densities in SOEC mode, pointing out that the depletion of H₂O at the TPB becomes substantial around -1 A/cm^2 . Here, our model indicates clearly, that the fuel electrode functional layer is the weakest part of the fuel electrode supported cell and has to be improved in its microstructure characteristics. Furthermore, the same conclusion can be made for the fuel electrode substrate. The nonlinear contributions of $\eta_{\text{conc,an}}$ and $\eta_{\text{act,an}}$ to the total polarization loss are deemed responsible for the observed asymmetry. This aspect is discussed in more detail in the next section. Corresponding results were reported by Knibbe et al.⁵⁵ using a $5 \times 5 \text{ cm}^2$ fuel electrode supported cell with YSZ/LSM oxygen electrode, identifying gas diffusion as a major source of asymmetry. Knibbe showed that gas conversion overvoltage, taking place in the gas channel above the fuel electrode substrate, was significant at high current densities. However, as this source of polarization loss is not considered in our model, it is not responsible for the observed asymmetry. This is bound to the fact that gas conversion losses are negligibly small for cells with an active area of 1 cm^2 operated at high gas flow rates as done in this work.

Gas diffusion overpotential at the fuel electrode ($\eta_{\text{conc,an}}$): Considering the above described scenario, in which the fraction of the gas, which is consumed in the electrochemical reaction is fixed, in

Eq. 12 the effective diffusion coefficients of H₂O, $D_{\text{H}_2\text{O}}^{\text{eff}}$, and H₂, $D_{\text{H}_2}^{\text{eff}}$, are the only values that differ, with $D_{\text{H}_2}^{\text{eff}} \approx 6.5 \times 10^{-5} \text{ m}^2/\text{s}$ almost double $D_{\text{H}_2\text{O}}^{\text{eff}} \approx 3.8 \times 10^{-5} \text{ m}^2/\text{s}$. This causes the gas diffusion overvoltage at the fuel electrode, $\eta_{\text{conc,an}}$, to be much larger in SOEC mode than in SOFC mode. As the binary diffusion coefficient for bulk diffusion is the same for H₂ diffusion in H₂O as for H₂O diffusion in H₂, bulk diffusion alone is symmetrical for both operation modes. Hence, the asymmetry in the diffusion overpotential for SOFC at current densities $\geq 2.4 \text{ A/cm}^2$ and SOEC mode at $\geq -1 \text{ A/cm}^2$ in turn proves that the Knudsen diffusion has to be taken into account for determining the diffusion overpotential of the fuel electrode of an electrode supported cell. It is agreed upon that Knudsen diffusion influences the transport of H₂O as this molecule is larger and heavier than the H₂ molecule.

Activation overpotential at the fuel electrode ($\eta_{\text{act,an}}$): To explain the influence of fuel electrode activation overvoltage, a closer look at Eq. 23 describing the exchange current density is necessary. It is a measure of the reaction rate and depends on the partial pressures of H₂ and H₂O. The exponents $a = -0.1$ (for p_{H_2}) and $b = 0.33$ (for $p_{\text{H}_2\text{O}}$) reveal that the smaller the $p_{\text{H}_2\text{O}}$ at the fuel electrode the lower the reaction rate of the electrochemical fuel oxidation, we refer to Table 1 or Ref. 2. Hence, the highest reaction rate is found for SOFC operation at high current densities and the lowest for SOEC operation at high current densities, respectively.

Therefore alongside an H₂O depletion for current densities $\geq 11 \text{ A/cm}^2$ in SOEC mode causing a large diffusion overvoltage at the fuel electrode – also the reaction rate decreases significantly, thereby causing a large activation polarization at the fuel electrode. Both processes have been nicely described by our model.

Applicability of the butler volmer (BV) approach for SOCs.—To discuss the adequacy of using the full BV in this work, C/V curves recorded at four different temperatures are shown in Fig. 12 (600...750°C, 62% H₂O). For comparison, the plot contains also linear C/V predictions, which are extrapolated on basis of the ASR

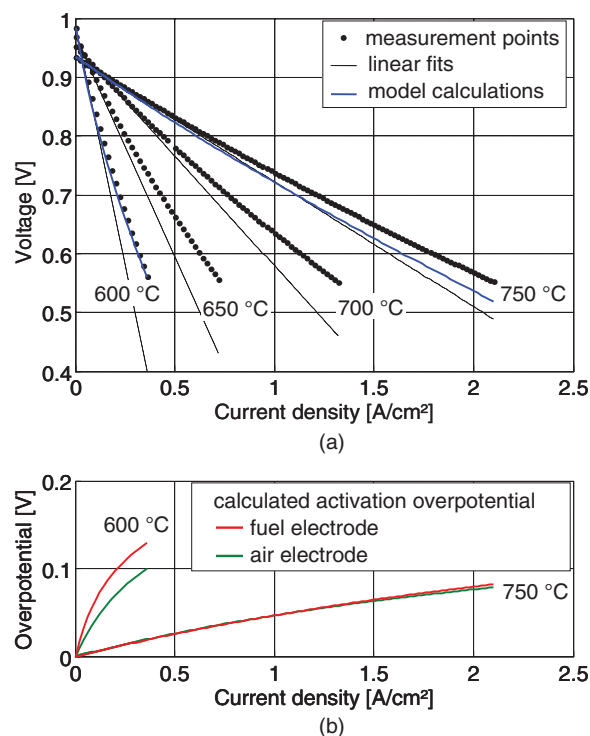


Figure 12. (a) Measured C/V curves at temperatures between 600°C and 750°C plus linear fits and (b) the activation overpotentials calculated by the proposed model.

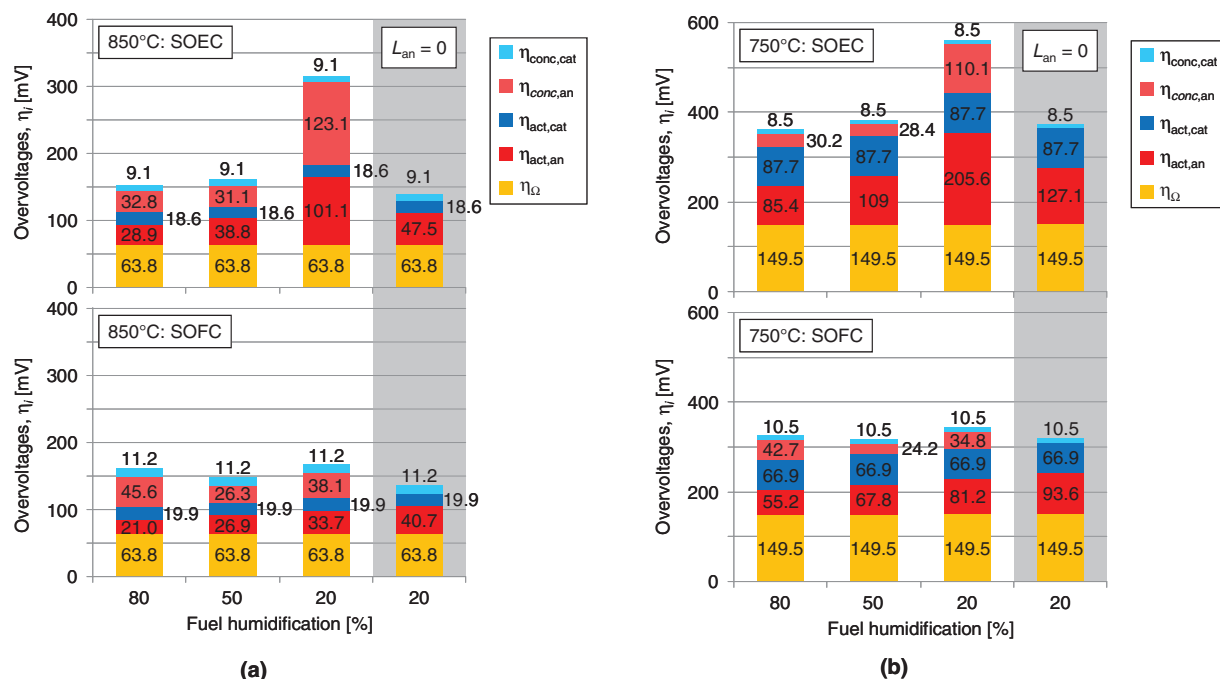


Figure 13. Simulation/predicted overvoltages for SOFC and SOEC modes for fuel electrode $p\text{H}_2\text{O}$ of 0.8, 0.5 and 0.2 atm, air (0.21 atm $p\text{O}_2$) at air electrode $p\text{O}_2$ at 1.5 A/cm² for: (a) 850°C and (b) 750°C.

at OCV for each measurement (dotted lines). For all temperatures, it is obvious that the measured C/V curves are nonlinear. Theoretically, both concentration polarization and activation polarization can be responsible for the observed nonlinear behavior. The former loss process shows minor temperature dependence and for the applied humidification of the fuel gas (62% H_2O), becomes nonlinear only for high current densities. The deviation of the measured C/V curves from the linear approximation however increases significantly for decreasing operating temperatures, where only small current densities are achieved. It is hence obvious that the thermally activated activation polarization has a significant contribution to the observed non-linearity of the measured C/V curves. The prediction based on our physically meaningful model hence shows excellent agreement with the measured data at low temperatures. At high temperatures, the model predictions are slightly lower than the measured C/V curves, however even here, the error is still smaller than for a linear prediction. Illustrating their non-linear contribution to the overall C/V curve, the activation overpotentials calculated by our model for fuel and air electrode, respectively, are depicted in Fig. 12b. These are small and show almost linear shape for the C/V curve at 750°C. For 600°C however, the activation overpotentials are much greater and their nonlinear C/V characteristic becomes obvious. In this light, it is proven that the fuel electrode supported cell type investigated herein, is insufficiently described by linear activation polarization overvoltages, when a wide range of operation conditions shall be predicted with a model.

Model predictions for selected conditions.—As mentioned previously, a good model has to be capable to assist the system developer in the choice of optimal operation point (e.g., temperature or electrode gas composition) and of operation mode, or to guide the cell manufacturer in further improving the cells for the desired operation mode. In Fig. 13a are model predictions of overvoltages resulting from individual loss mechanisms for operation at 850°C, fuel electrode steam partial pressures of 80-, 50- and 20% for both SOFC and SOEC operation at 1.5 A/cm². In Fig. 13b predictions for the same conditions for 750°C are shown.

Figure 13a reveals that at 850°C, at most gas compositions, and for both modes, the major performance limiting mechanism is the ionic conductivity of the electrolyte (including GDC and interdiffu-

sion layer) as depicted by the large ohmic losses (η_{ohm}). It can further be seen that only for operation with 80% H_2O the losses in SOEC mode are smaller than those in SOFC mode. With decreasing fuel humidification, the fuel electrode side losses in SOEC mode increase, becoming greater than the losses for SOFC mode. Hereby, the increasing overall overvoltages have to be attributed to an increase of both fuel electrode activation and concentration polarization for the above mentioned reasons. It is further interesting to see the coupling of both loss mechanisms. In any case, non-ideal gas diffusion leads to an accumulation of H_2O at the TPB in SOFC mode and to an H_2O depletion in SOEC mode. Therefore, the fuel electrode activation overvoltage, which increases significantly with decreasing $p\text{H}_2\text{O}_{\text{an}}$ (cf. Eqs. 22 and 23), is always greater in SOEC mode. Particularly for 20% H_2O , this effect becomes notable. Due to the non-ideal gas diffusion, the $p\text{H}_2\text{O}$ at the TPB is reduced to 0.019 atm at the TPB, resulting in a dramatically increased $\eta_{\text{act,an}}$. In the last columns of the diagram, the gas diffusion polarization in the substrate was not considered (i.e., the substrate thickness L_{an} was set to 10^{-15} m). Consequently, the predicted $p\text{H}_2\text{O}$ at the TPB is constant at 0.2 atm and as a result, fuel electrode activation polarization in SOEC mode is decreased from 101 mV (with gas diffusion polarization) to 48 mV (without gas diffusion polarization). For SOFC operation, the constant $p\text{H}_2\text{O}_{\text{an}}$ has a negative impact on the activation overvoltage. Accordingly, the model without gas diffusion polarization reveals an increased fuel electrode activation polarization of 41 mV compared to 34 mV with gas diffusion polarization.

From Fig. 13b in which the 750°C situation is predicted, similar trends to those at 850°C can be observed. Except for SOEC mode with $p\text{H}_2\text{O} = 0.2$ atm, the concentration overpotentials per se do not represent a major contribution to the overall overvoltages of the cell. Gas diffusion still plays an important role at 750°C, where the thermally activated activation overvoltages are more pronounced and hence the impact of gas diffusion on the activation polarization becomes more significant. The latter translates to greater differences in $\eta_{\text{act,an}}$ for SOFC and SOEC mode and, as a result, the overall overvoltages in SOEC mode are always higher than in SOFC mode.

These results show that there is a strong coupling of gas diffusion and activation polarization.

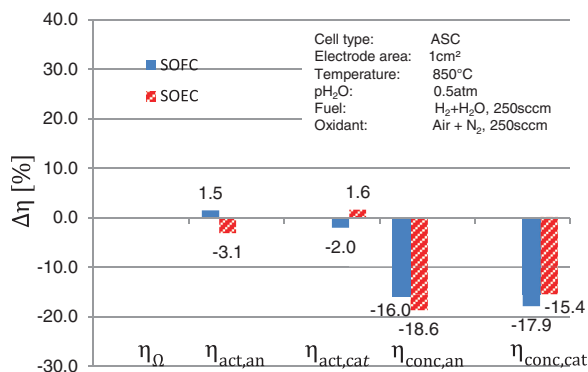


Figure 14. Simulated/predicted overvoltages for SOFC and SOEC modes for porosity : tortuosity ratios (structural parameter) for a relative changes in ASR due to a 20% decrease in ψ_{el} .

For the loss mechanisms of the cells analyzed herein, this coupling plays an important role, particularly in SOEC operation. It is hence important for this operation mode to improve gas transport properties at the fuel electrode. As discussed above, fuel-side gas transport is represented by gas diffusion of H_2/H_2O , mainly through the porous fuel electrode support. From Eqs. 12 and 14, it is obvious that fuel-side gas transport properties can be improved by either thinner thickness of the electrode support (L_{an}) or improved microstructure (represented by the parameter ψ_{an}). The predictive power of the model is illustrated exemplarily in Fig. 14, where the impact of the electrode microstructures on the single polarization overvoltages is discussed for SOFC and SOEC operation at 850°C , 1.5 A/cm^2 , $p_{H_2O} = 0.5 \text{ atm}$ and $p_{O_2} = 0.21 \text{ atm}$ (original overvoltages are represented in Fig. 13a). Figure 14a gives the impact of an increased ψ_{el} by 20% on the single polarization overpotentials. The increase in ψ_{el} corresponds to an increase in porosity of 20% or a decrease in tortuosity of 16.7% in the corresponding electrode (cf. Eq. 15). The improved fuel-side diffusion polarization contributions (−19% for SOEC and −16% for SOFC operation) can be seen immediately. Improved activation of the fuel electrode, though to a smaller degree (−3%), is also observed for SOEC operation, whereas an expectedly adverse impact (of 1.5%) is observed for SOFC operation. It has to be noted that at lower operating temperatures, the thermally activated activation polarization losses are more pronounced (cf. Fig. 13b) and hence a greater impact of gas diffusion on $\eta_{act,an}$ is expected.

Also at the air electrode, an increase of 20% on ψ_{el} causes an improvement in diffusion overpotential for both SOFC and SOEC modes. But contrary to the fuel electrode, SOFC operation benefits more (−18% vs. −15% for SOEC). Also the air electrode activation polarization shows an improvement of −2% in SOFC operation and an increase of 1.6% in activation polarization for SOEC operation mode.

The explanation for all of the discussed points and differences are centered around the fact that the H_2O molecule is larger than the H_2 molecule and has a smaller Knudsen diffusion coefficient as well. Since H_2O is fuel in SOEC mode, the impact on SOEC operation is generally greater in either direction. Since activation polarization is related to the exchange current density, which in turn is dependent on the gas concentrations at the TPB, activation is as well affected by changes in ψ_{el} . Naturally, the impact of other parameters such as substrate thickness, mean pore diameter, electrolyte thickness on the cell performance can be predicted by the model as well.

Conclusion

It could be shown that our zero-dimensional and isothermal stationary model originally developed for the prediction of C/V characteristics of fuel electrode supported single cells in SOFC mode, describes the C/V characteristics of reverse SOEC operation as well.

The asymmetry of dual mode operation, revealed in the C/V characteristics, namely the higher losses for high current densities in SOEC mode, is proven by experiments. This effect is explained by (i) increasing polarization losses related to Knudsen diffusion and (ii) decreasing reaction rate in dry conditions at the fuel electrode at high current densities in SOEC mode. It is also shown, that modeling the activation overvoltage with the full Butler-Volmer equation for SOFC or SOEC operation - though theoretically debatable matches very well with the experimentally determined activation overvoltage. As a C/V measurement is accompanied by temperature change inside the cell, our model is further enhanced by including the actual cell temperature determined through a new impedance-based temperature measurement routine.

After demonstrating the accuracy of the model over a broad range of operating parameters in SOFC and SOEC mode, the model can be applied in order to identify ideal operating parameters as well as investigating the potential of further developments in cell design.

The consistent results achieved for steam electrolysis with the revised temperature-dependent model, encourage us to investigate its applicability for (i) the electrolysis of Carbon dioxide and (ii) the co-electrolysis of carbon dioxide and steam in future experiments.

Acknowledgments

The authors gratefully acknowledge the trusting collaboration with Forschungszentrum Jülich, where the fuel electrode supported cells are successfully developed for SOFC operation since more than twenty years. Thanks to Michael Kornely for valuable discussions and to Christian Gabi, Torsten Johannsen and Stefan Ziegler for continuous assistance in the laboratory.

References

1. A. Leonide, V. Sonn, A. Weber, and E. Ivers-Tiffée, *J. Electrochem. Soc.*, **155**(1), B36 (2008).
2. A. Leonide, Y. Apel, and E. Ivers-Tiffée, *ECSS Trans.*, **19**(20), 81 (2009).
3. J. Udagawa, P. Aguiar, and N. P. Brandon, *J. Power Sources*, **166**(1), 127 (2007).
4. J. Udagawa, P. Aguiar, and N. P. Brandon, *J. Power Sources*, **180**(1), 46 (2008).
5. M. Ni, M. K. H. Leung, and D. Y. C. Leung, *International Journal of Hydrogen Energy*, **32**(13), 2305 (2007).
6. M. Ni, *Chemical Engineering Journal*, **164**(1), 246 (2010).
7. M. Ni, *International Journal of Hydrogen Energy*, **34**(18), 7795 (2009).
8. J. S. Herring, J. E. O'Brien, C. M. Stoots, G. L. Hawkes, J. J. Hartvigsen, and M. Shahnam, *International Journal of Hydrogen Energy*, **32**(4), 440 (2007).
9. J. Laurencin, D. Kane, G. Delette, J. Deseure, and F. Lefebvre-Joud, *J. Power Sources*, **196**(4), 2080 (2011).
10. M. Ni, *International Journal of Hydrogen Energy*, **37**(8), 6389 (2012).
11. C. Endler, A. Leonide, A. Weber, F. Tietz, and E. Ivers-Tiffée, *J. Electrochem. Soc.*, **157**(2), B292 (2010).
12. C. H. Hamann, A. Hamnett, and W. Vielstich, *Electrochemistry*, 2 ed., Wiley-VCH, Weinheim (2007).
13. C. Endler-Schuck, A. Weber, E. Ivers-Tiffée, U. Guntow, J. Ernst, and J. Ruska, *Journal of Fuel Cell Science and Technology*, **8**(4), 041001-1 (2011).
14. D. Sanchez, R. Chacartegui, A. Munoz, and T. Sanchez, *J. Power Sources*, **160**(2), 1074 (2006).
15. A. C. Müller, J. R. Opfermann, and E. Ivers-Tiffée, *Thermochimica Acta*, **414**(1), 11 (2004).
16. S. Prindahl and M. Mogensen, *J. Electrochem. Soc.*, **146**(8), 2827 (1999).
17. J. W. Kim, A. V. Virkar, K. Z. Fung, K. Mehta, and S. C. Singhal, *J. Electrochem. Soc.*, **146**(1), 69 (1999).
18. A. V. Virkar, J. Chen, C. W. Tanner, and J. W. Kim, *Solid State Ionics*, **131**(1–2), 189 (2000).
19. E. A. Mason and A. P. Malinauskas, *Gas Transport in Porous Media: The dusty gas Model*, Elsevier, Amsterdam (1983).
20. R. Jackson, *Transport in porous catalysts*, Elsevier, Amsterdam (1977).
21. A. V. Akkaya, *Int. J. Energy Res.*, **31**(1), 79 (2007).
22. E. L. Cussler, *Diffusion: Mass Transfer in Fluid Systems*, Cambridge University Press, Cambridge (1984).
23. B. Poling, J. M. Prausnitz, and J. P. O'Connell, *The properties of gases and liquids*, 5. ed. ed., McGraw-Hill, New York [u.a.] (2001).
24. A. Leonide, S. Ngo Dinh, A. Weber, and E. Ivers-Tiffée, in *Proceedings of the 8th European Solid Oxide Fuel Cell Forum*, R. Steinberger-Wilckens and U. Bossel, Editors, p. A0501 (2008).
25. S. B. Adler, J. A. Lane, and B. C. H. Steele, *J. Electrochem. Soc.*, **143**(11), 3554 (1996).
26. T. Carraro, J. Joos, B. Rüger, A. Weber, and E. Ivers-Tiffée, *Electrochimica Acta*, **77**, 315 (2012).

27. P. Aguiar, C. S. Adjiman, and N. P. Brandon, *J. Power Sources*, **138**(1–2), 120 (2004).
28. Y. Wang, F. Yoshiba, T. Watanabe, and S. L. Weng, *J. Power Sources*, **170**(1), 101 (2007).
29. D. A. Noren and M. A. Hoffman, *J. Power Sources*, **152**(1), 175 (2005).
30. R. F. Mann, J. C. Amphlett, B. A. Peppley, and C. P. Thurgood, *J. Power Sources*, **161**(2), 775 (2006).
31. J. O'M. Bockris and Z. Nagy, *Journal of Chemical Education*, **50**(12), 839 (1973).
32. R. J. Gorte and J. M. Vohs, *Annu. Rev. Biomol. Eng.*, **2**, 9 (2011).
33. M. Ni, *J. Power Sources*, **202**, 209 (2012).
34. S. Campanari and P. Iora, *J. Power Sources*, **132**(1–2), 113 (2004).
35. W. Jiang, R. X. Fang, J. A. Khan, and R. A. Dougal, *J. Power Sources*, **162**(1), 316 (2006).
36. V. Sonn, A. Leonide, and E. Ivers-Tiffée, *J. Electrochem. Soc.*, **155**(7), B675 (2008).
37. W. G. Bessler, M. Vogler, H. Störmer, D. Gerthsen, A. Utz, A. Weber, and E. Ivers-Tiffée, *Phys. Chem. Chem. Phys.*, **12**, 13888 (2010).
38. S. Gewies and W. G. Bessler, *J. Electrochem. Soc.*, **155**(9), B937 (2008).
39. W. G. Bessler, S. Gewies, and M. Vogler, *Electrochimica Acta*, **53**(4), 1782 (2007).
40. V. Yurkiv, A. Utz, A. Weber, E. Ivers-Tiffée, H. R. Volpp, and W. G. Bessler, *Electrochimica Acta*, **tbd**(0), tbd (2011).
41. S. B. Adler and W. G. Bessler, in *Handbook of Fuel Cells - Fundamentals, Technology and Applications*, W. Vielstich, H. Yokokawa, and H. A. Gasteiger, Editors, p. 441, John Wiley & Sons Ltd, Chichester (2009).
42. K. V. Jensen, R. Wallenberg, I. Chorkendorff, and M. Mogensen, *Solid State Ionics*, **160**(1–2), 27 (2003).
43. M. S. Schmidt, K. V. Hansen, K. Norrman, and M. Mogensen, *Solid State Ionics*, **179**(27–32), 1436 (2008).
44. A. Utz, K. V. Hansen, K. Norrman, E. Ivers-Tiffée, and M. Mogensen, *Solid State Ionics*, **183**(1), 60 (2011).
45. B. Rüger, J. Joos, T. Carraro, A. Weber, and E. Ivers-Tiffée, *ECS Trans.*, **25**(2), 1211 (2009).
46. A. Utz, H. Störmer, A. Leonide, A. Weber, and E. Ivers-Tiffée, *J. Electrochem. Soc.*, **157**(6), B920 (2010).
47. A. J. Bard and L. R. Faulkner, *Electrochemical Methods Fundamentals and Applications*, John Wiley & Sons, Inc., New York (2001).
48. N. Menzler, W. Schafbauer, F. Han, O. Büchler, R. Mücke, H. P. Buchkremer, and D. Stöver, *Materials Science Forum*, **654–656**, 2875 (2010).
49. D. Stöver, H. P. Buchkremer, and J. P. P. Huijsmans, in *Handbook of Fuel Cells*, W. Vielstich, A. Lamm, and H. A. Gasteiger, Editors, p. 1015, John Wiley & Sons Ltd., Chichester, UK (2003).
50. M. Becker, A. Mai, E. Ivers-Tiffée, and F. Tietz, in *Proceedings of the Ninth International Symposium on Solid Oxide Fuel Cells (SOFC IX)*, S. C. Singhal and J. Mizusaki, Editors, **1**, p. 514 (2005).
51. A. Mai, M. Becker, W. Assenmacher, F. Tietz, D. Hathiramani, E. Ivers-Tiffée, D. Stöver, and W. Mader, *Solid State Ionics*, **177**(19–25), 1965 (2006).
52. D. Klotz, A. Weber, and E. Ivers-Tiffée, in *Proceedings of the 8th European Solid Oxide Fuel Cell Forum*, R. Steinberger-Wilckens and U. Bossel, Editors, p. B0909 (2008).
53. D. Klotz, J. C. Njodzefon, A. Weber, and E. Ivers-Tiffée, *ECS Trans.*, **45**(1), 523 (2012).
54. C. Peters, A. Weber, B. Butz, D. Gerthsen, and E. Ivers-Tiffée, *J. Am. Ceram. Soc.*, **92**(9), 2017 (2009).
55. R. Knibbe, M. Lund Traulsen, A. Hauch, S. Dalgaard Ebbesen, and M. Mogensen, *J. Electrochem. Soc.*, **157**, B1209 (2010).